Device

Article

Wavelength-selective photodetectors with high quantum efficiency using an optical blocking layer and a field-induced junction on a silicon nanowire

Graphical abstract

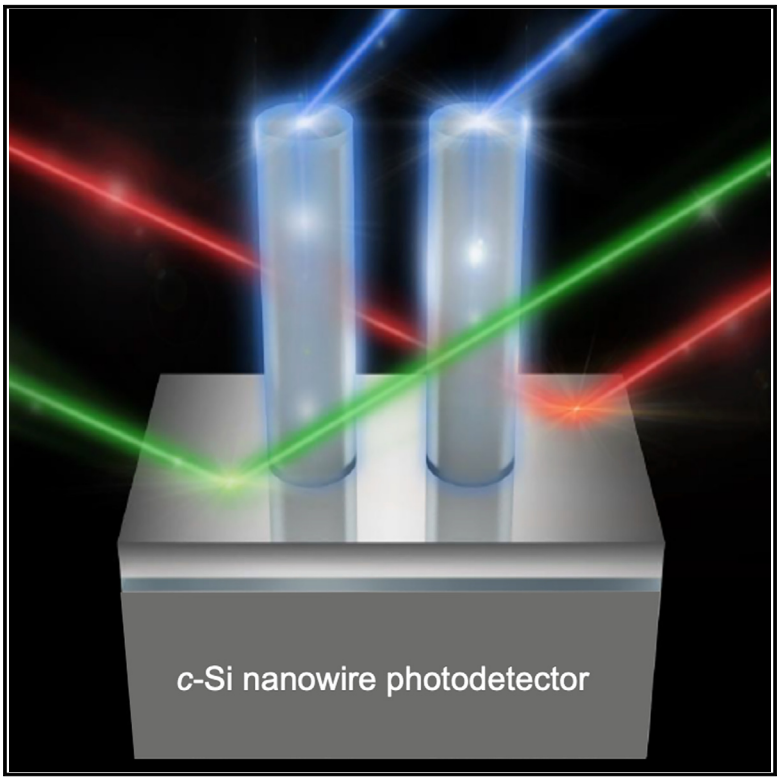

Highlights

- The highest EQE (77.4%) among *c*-SiNW photodetectors is achieved using ALD-Al_2O_3
- The selectivity of *c*-SiNW photodetector is improved by a novel optical blocking layer
- High-performance UV and NIR photodetectors can be achieved by our device architecture

Authors

Deokjae Choi, Jungtaek Lee, Munib Wober, Young-Ki Kim, Han-Don Um, Kwanyong Seo

Correspondence

kseo@unist.ac.kr

In brief

Crystalline silicon nanowires (*c*-SiNWs) are promising candidates for next-generation photodetectors in UV, visible, and NIR regions owing to their unique optical properties. However, reported *c*-SiNW photodetectors have so far been limited by their low external quantum efficiency (EQE) and selectivity. Here, we demonstrate a *c*-SiNW photodetector with a 77.4% EQE using a novel optical blocking layer and a field-induced junction. This is a significant achievement over previously reported studies (<30%).

Choi et al., 2023, Device *1*, 100018
August 25, 2023
https://doi.org/10.1016/j.device.2023.100018

CellPress

Device

CellPress
OPEN ACCESS

Article

Wavelength-selective photodetectors with high quantum efficiency using an optical blocking layer and a field-induced junction on a silicon nanowire

Deokjae Choi,[1,5] Jungtaek Lee,[1,5] Munib Wober,[1] Young-Ki Kim,[2] Han-Don Um,[3] and Kwanyong Seo[1,4,6,*]

[1]School of Energy and Chemical Engineering, Ulsan National Institute of Science and Technology (UNIST), Ulsan 44919, Republic of Korea
[2]UNIST Central Research Facilities, Ulsan National Institute of Science and Technology (UNIST), Ulsan 44919, Republic of Korea
[3]Department of Chemical Engineering, Kangwon National University, Chuncheon, Gangwon-do 24341, Republic of Korea
[4]Graduate School of Carbon Neutrality, Ulsan National Institute of Science and Technology (UNIST), Ulsan 44919, Republic of Korea
[5]These authors contributed equally
[6]Lead contact
*Correspondence: kseo@unist.ac.kr
https://doi.org/10.1016/j.device.2023.100018

THE BIGGER PICTURE Crystalline silicon nanowires (*c*-SiNWs) are expected to be next-generation photodetectors enabling filter-free and highly integrated multispectral photodetection. In this study, we present the fabrication of a *c*-SiNW photodetector with an EQE of 77.4% and remarkable wavelength selectivity by employing a field-induced junction and an optical blocking layer on *c*-SiNWs. This is a significant achievement in the photodetector research field, as the EQE is dramatically increased compared with those in previously reported studies (<30%). In the longer term, this research could lead to the development of high-sensitivity and high-selectivity UV and NIR photodetectors with diameter-controllable *c*-SiNWs, which will have a significant and broad implication on optoelectronic research and various industry fields.

SUMMARY

Crystalline silicon nanowires (*c*-SiNWs) have unique optical characteristics that enable tuning of their spectral response. However, real-world applications of *c*-SiNWs as multispectral photodetectors are still hampered by their low selectivity and low quantum efficiency (<30%). The primary obstacles include the broad-spectrum light absorption of the bottom crystalline silicon (*c*-Si) substrate underneath the *c*-SiNWs and the difficulties in forming appropriate *p*-*n* junctions on *c*-SiNWs. In this study, an optical blocking layer was applied to block light absorption in the bottom *c*-Si substrate, and atomic-layer deposition-based Al_2O_3 was employed to form a dopant-free *p*-*n* junction on diameter-controlled *c*-SiNWs. Consequently, the maximum external quantum efficiency (EQE) of the fabricated photodetector is 77.4% with remarkable wavelength selectivity. This work removes major stumbling blocks for the use of *c*-SiNWs as selective light spectral band-pass photodetectors.

INTRODUCTION

Crystalline silicon nanowires (*c*-SiNWs) have attracted much attention for use in solar cells, nanoelectronics, and photodetectors owing to their unique optical and electrical characteristics, which are not observed in their bulk form.[1–7] In particular, *c*-SiNWs exhibit diameter-dependent, wavelength-selective waveguide modes and attendant light absorption. The spectral response can be easily tuned in the full range of the visible spectrum by controlling the diameter of the wire.[8] Despite the superior ability to tune their spectral response, low selectivity and low quantum efficiency (<30%) are significant limitations for *c*-SiNWs in photodetector applications. First, the bottom crystalline silicon (*c*-Si) substrate that supports the *c*-SiNW absorbs light and generates carriers in a broad wavelength range, deterring the desired spectral selectivity of the *c*-SiNW-based photodetector.[9] A bottom *c*-Si substrate is necessary for carrier transport, extraction, and handling of the sample during device fabrication. Previous work that aimed to solve this problem stacked a *c*-SiNW (doped $p^+/i/n^+$) photodetector on a planar (doped $n^+/i/p^+$) photodetector, followed by the application of an external bias.[10] Applying a negative voltage to the top contact causes the nanowire and planar photodetectors to be under reverse and forward biases, respectively. Therefore, the final photocurrent only originates from light absorption in the *c*-SiNWs. However, external power must be applied to operate

the device continuously. For practical applications, it is necessary to generate a photocurrent that originates from light absorption in *c*-SiNWs without an external bias. Second, it is challenging to form appropriate *p*-*n* junctions on the *c*-SiNWs. Conventional thermal doping or ion implantation results in severe Auger recombination and numerous lattice defects in *c*-SiNWs[11,12]; consequently, the external quantum efficiency (EQE) of the photodetector decreases significantly. Therefore, an alternative approach is required to form a *p*-*n* junction on *c*-SiNWs for a high EQE.

This study suggests a novel strategy for blocking the electrical response from the bottom substrate by fundamentally preventing the light absorption by the substrate. We observed that the bottom substrate absorption is primarily caused by photons entering the substrate in the spaces between *c*-SiNWs. To prevent the incident light from reaching the substrate, an optical blocking layer was employed on the spaces between the *c*-SiNWs. Through finite-difference time-domain (FDTD) simulation, we establish that the optical blocking layer successfully blocks the incident light, which can be absorbed by the bottom substrate. Finally, a photodetector device was fabricated by coating a negatively charged Al_2O_3 layer via atomic layer deposition (ALD) to form a dopant-free *p*-*n* junction. The negatively charged Al_2O_3 layer on *n*-type *c*-Si has been extensively studied as an alternative for the conventional thermal doping process.[13–15] Here, we prove that ALD-based Al_2O_3 is a promising candidate for forming *p*-*n* junctions on wavelength-selective *c*-SiNWs by demonstrating a high EQE of 77.4%. To the best of our knowledge, this is the highest value among those previously reported for *c*-SiNW-based multispectral photodiodes at zero bias (Table S1). Moreover, the selectivity of the photodetector with an optical blocking layer is dramatically improved compared with that of the device without an optical blocking layer. In other words, the fabricated photodetector with an optical blocking layer successfully removed the confounding substrate contribution.

RESULTS

Optimization of physical dimension of *c*-SiNW arrays

To maximize the wire absorption for a high EQE, we examined the wire absorption trend by varying the physical dimensions (wire length and pitch) of *c*-SiNWs via FDTD simulation. Figure 1A shows the schematic of the *c*-SiNW array used in the FDTD simulation. We applied 10 nm Al_2O_3 onto the *c*-SiNW surface to form a field-induced *p*-*n* junction, which will be discussed later. As a simulation result, the wire absorption and the substrate absorption of *c*-SiNW were separately obtained. As expected, the reflection dips were systematically shifted over the full range of the visible spectrum when the diameter of the *c*-SiNW was adjusted from 90 to 140 nm (Figures 1B and 1C).[8] The wire length was varied from 1 to 5 μm by fixing the wire pitch at 1 μm and the wire diameter at 90 nm (Figures 1D and 1E). As the wire length increases, the wire absorption is enhanced, indicating that increasing the wire length is an effective strategy to improve the wire absorption. However, there is a practical limit to increasing the wire length because it is challenging to experimentally increase the aspect ratio of the *c*-SiNW while maintaining the cylindrical shape of the wire, which has a nanometer-scale diameter. As the etching time increases, it becomes progressively difficult for the etching gas or solution to consistently penetrate to the deep wire spacing; consequently, the *c*-SiNW array has a tapered shape, which results in a broad spectrum.[16] In other words, considering the fabrication of *c*-SiNWs, it is necessary to find another approach to maximize wire absorption with an achievable wire length. The remaining parameter that can be considered is the wire pitch. Considering the feasibility of cylindrical wire fabrication, the wire length was fixed at 2 μm (aspect ratio ≈ 1:20). The wire pitch was adjusted from 1 μm to 300 nm, while the wire diameter was fixed at 90 nm (Figures 1F and 1G). As the wire pitch decreases, wire absorption is significantly enhanced. This is because the number of wires that can absorb incident light per unit area increases as the wire pitch decreases. However, as the pitch decreases below 700 nm, the light absorption on the short-wavelength region increases significantly. This can be explained by the evanescent mode coupling between neighboring wires.[8] However, there is no change in the wire absorption in the long-wavelength region, over 570 nm, where *c*-SiNWs with a diameter of 90 nm do not absorb. Notably, the absorption spectrum gets significantly broader as the wire pitch decreases below 400 nm. Therefore, the optimal range of the wire pitch can be considered between 500 and 700 nm in terms of the maximum absorption peak and the selectivity. In this work, the optimized wire pitch was chosen to be 700 nm (Figure S1).

FDTD simulation of optical blocking layer

An optical blocking layer was designed to utilize the bottom *c*-Si substrate while preventing substrate absorption. Figure 2A illustrates the schematics of the optical blocking layer that formed on the *c*-Si substrate and between *c*-SiNW spaces. This is because the time-dependent video of light propagation on *c*-SiNWs confirms that the photons passing between *c*-SiNW spaces are absorbed by the bottom *c*-Si substrate (Video S1). As an optical blocking layer, we applied Al metal, which is commonly used in optical mirrors in the visible wavelength region. Figures 2B and 2C depict the simulated total absorption spectra (i.e., the sum of the wire absorption and substrate absorption) of *c*-SiNWs without and with Al metal, respectively. The wire diameters were varied from 90 to 130 nm, and the length and pitch of the wires are 2 μm and 700 nm, respectively. Compared with *c*-SiNWs without Al metal, the selectivity for total absorption with Al metal is significantly improved. Moreover, we calculated the full width at half maximum (FWHM), which is the difference between the two independent variables when the dependent variable is equal to half of its maximum value. Without Al metal, the FWHM cannot be obtained because of the broad absorption of the bottom *c*-Si substrate (Figure 2D). For Al metal, the calculated FWHM values are 74, 98, and 83 nm for wire diameters of 90, 110, and 130 nm, respectively (Figure 2E). The results indicate that the selectivity of the absorption spectra greatly improved after the application of an optical blocking layer. This can be explained by the significant reduction in the substrate absorption by the optical blocking layer, as shown in Figures 2F and 2G. The substrate absorption was dramatically reduced after the application of Al metal. The average absorption of the *c*-Si substrate decreased from 60.8% to 6.3% when Al metal was used.

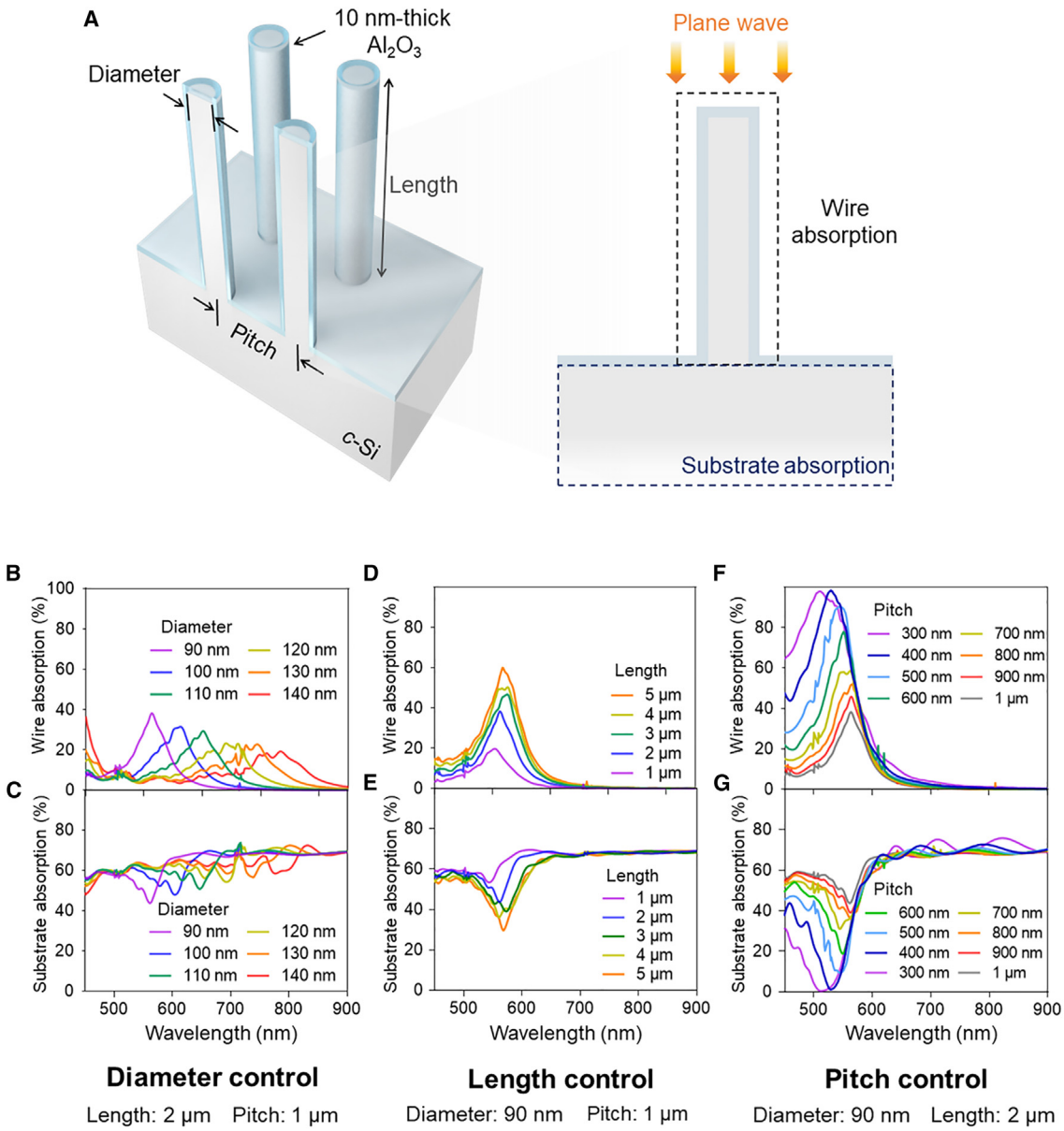

Figure 1. Optimization of physical dimension of *c*-SiNW array

(A) Schematic showing the *c*-SiNW array used in the FDTD simulation.

(B–G) Simulated wire and substrate absorption spectra according to different wire diameters (B and C), lengths (D and E), and pitches (F and G), respectively.

Therefore, Al metal effectively blocked 89.6% of the incident light absorbed by the bottom substrate.

Comparison between Al metal and perfect reflector as an optical blocking layer

A residual substrate absorption of 10.4% exists when an Al metal blocking layer was used. An additional FDTD simulation was conducted to gain a comprehensive understanding of the optical phenomenon that occurs when the optical blocking layer is used. We compared the blocking ability of Al metal with an ideal perfect reflector. As a perfect reflector, a perfect electric conductor (PEC) was employed as the optical blocking layer. In FDTD simulations, the PEC is an ideal material exhibiting infinite electrical conductivity. Since the electric field inside the conductor is consistently zero, electromagnetic energy does not pass through the PEC. Consequently, the PEC reflects all the energy of the incident light.[17,18] The refractive index *n* and *k* values of the PEC used in this study are provided in Figure S2. Figure 2H shows the total absorption separated into wire and bottom substrate absorption when the PEC was used as the optical blocking layer. The PEC layer significantly reduced the substrate absorption in a broad wavelength region from 450 to 900 nm, demonstrating a 94.8% reduction in the total integrated photons absorbed by the substrate. Even when a perfect reflector (PEC layer) was used, a

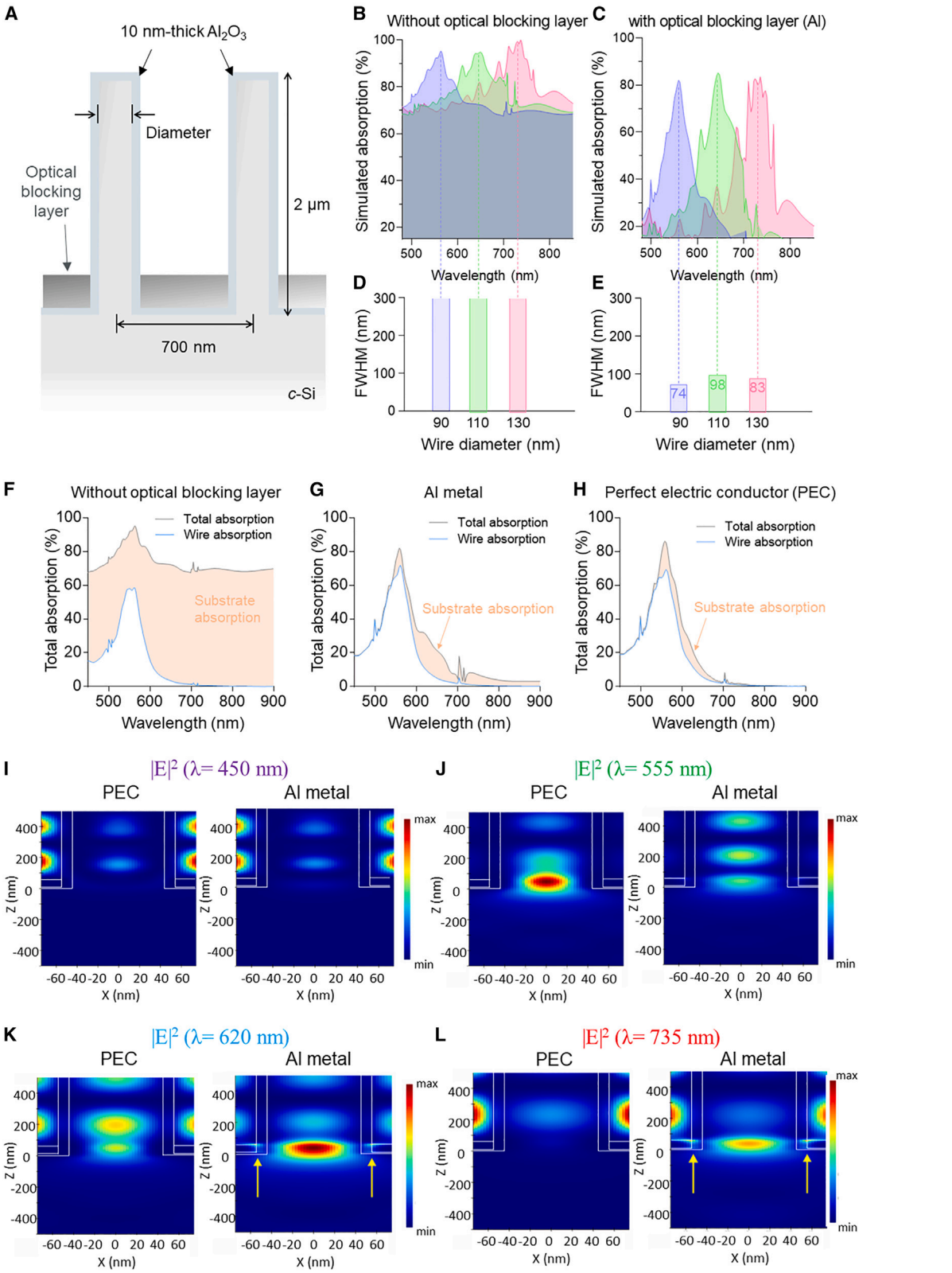

(legend on next page)

substrate absorption of 5.2% was observed. The light guided into the *c*-SiNW is not completely absorbed by the *c*-SiNW and evanesces the bottom *c*-Si substrate. This can be observed in the time-dependent video of light propagation on *c*-SiNWs with the PEC layer (Video S2). Since only light guided into the *c*-SiNW can reach the bottom substrate, the wavelength range of substrate absorption did not exceed 700 nm, which is outside the wavelength range of the wire absorption.

In contrast, Al metal (89.6%) exhibited a relatively lower light-blocking ability than the ideal PEC layer (94.8%). Additionally, the wavelength range of substrate absorption exceeded 700 nm, which is outside the wavelength range of wire absorption. To further investigate this unique optical behavior of Al metal, 2D electric field intensity plots in the vertical cross-section of *c*-SiNWs with Al metal were obtained. Figures 2I and 2J illustrates the 2D electric field intensity profiles at different wavelengths (450 and 555 nm). In the case of the 450-nm-wavelength light, an electric field close to zero was observed in the bottom substrate with both the PEC layer and Al metal. Most of the light outside the *c*-SiNW was reflected, and the light propagating inside the *c*-SiNW was primarily absorbed through the wire. At a wavelength of 555 nm, substrate absorption occurred in both the Al metal and PEC layers. As shown in the electric field intensity profile, the light passing through the *c*-SiNW reached the bottom substrate and was absorbed by the bottom substrate. However, at a wavelength of 620 nm (Figure 2K), surface plasmon resonance (indicated by yellow arrows) was observed when Al metal was used. Consequently, the electric field intensity at the bottom substrate was further enhanced compared with that of the PEC layer. At a wavelength of 735 nm (Figure 2L), the surface plasmon resonance was observed only when Al metal was employed. Consequently, the PEC layer (0.5%) exhibits smaller substrate absorption compared with the Al metal (7.2%) at a wavelength of 735 nm. Even though Al metal (89.6%) exhibits a relatively lower blocking ability than the perfect reflector (94.8%), the wire absorption and selectivity could be dramatically improved by using an Al blocking layer. Therefore, Al metal is a good candidate for the realization of an optical blocking layer.

Fabrication process of optical blocking layer

As designed in the optical simulation, it is crucial to experimentally form Al metal only between the *c*-SiNW spaces, not on the top or sidewalls of the wires. In Figure 3A, schematics of the fabrication process of the vertical *c*-SiNW arrays with an Al metal layer are shown. First, Al metal dot patterns were formed on a *c*-Si substrate via e-beam lithography and subsequent thermal evaporation processes. Subsequently, Al metal dots were used as an etch mask for fabricating vertical *c*-SiNW arrays via a deep reactive ion etching (DRIE) method. Following the deposition of ALD-Al_2O_3 on the surface of the vertical *c*-SiNW arrays, an Al metal film was formed on the sample via thermal evaporation to form the optical blocking layer. Although the thermal evaporation process is highly directional compared with other chemical vapor deposition methods, such as ALD and plasma-enhanced chemical vapor deposition (PECVD), Al metal is inevitably coated on the flat top or sidewalls of *c*-SiNWs.[19] A photoresist (PR) layer was used to selectively remove the Al metal deposited on the top or sidewalls of *c*-SiNWs. The thickness of the PR layer coated onto *c*-SiNWs was controlled by the oxygen plasma etching time, and the remaining PR acted as a protection layer from the Al etchant. The top and sidewalls of *c*-SiNWs, except for the bottom part, were selectively exposed to air. Following oxygen plasma etching, the Al metal on the top and sidewalls of *c*-SiNW was selectively removed by an Al etchant. Finally, the PR layer was removed by plasma etching.

Scanning electron microscope (SEM) measurements were performed to confirm that Al metal remained only between *c*-SiNW spaces. Figure 3B shows a SEM image of the fabricated *c*-SiNW array with Al metal as the optical blocking layer. The measured wire diameter, pitch, and length were 90 nm, 700 nm, and 2 μm, respectively. SEM images for other wire diameters (110 and 130 nm) are shown in Figure S3. Moreover, we obtained high-magnification SEM images of the top and bottom of the *c*-SiNW, respectively (Figures 3C and 3D). Consequently, we confirmed that Al metal was successfully formed only between the *c*-SiNW spaces and not on the top or sidewalls of the wires, as designed in the optical simulation. High-magnification SEM images of the top and bottom of *c*-SiNW before and after the Al etching process are also provided in Figure S4. In this study, a high-quality 10-nm-thick Al_2O_3 layer was coated onto the *c*-SiNW via ALD for field-induced junctions and surface passivation, which are discussed in Figure 4. A high-resolution transmission electron microscope (TEM) image of the interface between the *c*-SiNW wall and the ALD-based Al_2O_3 was obtained. In addition, energy-dispersive X-ray spectroscopy (EDS) revealed that the Al_2O_3 layer uniformly covered the surface of the *c*-SiNW (Figure S5). The crystal structures of *c*-SiNWs and Al_2O_3 were examined using fast Fourier transform (FFT) images (Figure 3E). The clear FFT image displayed in the inset of Figure 3E shows the highly crystalline nature of the *c*-SiNW. In the case of Al_2O_3, the amorphous nature is more dominant than the crystalline nature compared with *c*-SiNWs. ALD-Al_2O_3 is known to exhibit strong crystallinity after post-annealing over 800°C.[20]

Characterization of *c*-SiNW-based photodetector with optical blocking layer

c-SiNW-based photodetector devices were fabricated by forming a *p-n* junction and metal electrodes. It is known that thermal

Figure 2. FDTD simulation of *c*-SiNW array with an optical blocking layer

(A) Schematic of an optical blocking layer (Al metal) formed on the *c*-Si substrate and between *c*-SiNW spaces.

(B and C) The simulated total absorption (B) without and (C) with an optical blocking layer (Al metal) for different wire diameters. Notably, the total absorption is the sum of the wire absorption and substrate absorption.

(D and E) The full width half maximum (D) without and (E) with an optical blocking layer for different wire diameters.

(F–H) Simulated total and wire absorption (F) without optical blocking layer, (G) with Al metal, and (H) with a perfect electric conductor.

(I–L) The square of the electric field profile when the PEC layer and Al metal are applied to the *c*-SiNW at different wavelengths: (I) 450 nm, (J) 555 nm, (K) 620 nm, and (L) 735 nm, respectively.

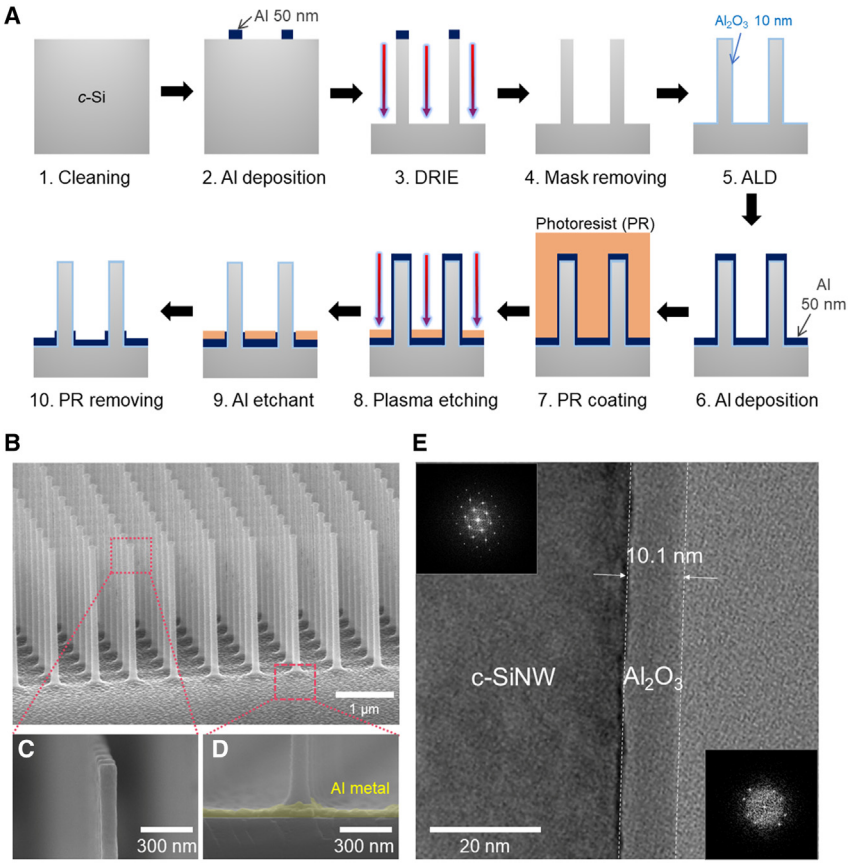

Figure 3. Fabrication process and electron microscope images of *c*-SiNW arrays with ALD-Al_2O_3 and optical blocking layer

(A) Fabrication process for applying Al metal (optical blocking layer) to the *c*-Si substrate and between *c*-SiNW spaces.

(B) Scanning electron microscope (SEM) image that shows the fabricated *c*-SiNW with Al metal as an optical blocking layer.

(C and D) High-magnification SEM images for (C) top and (D) bottom of the *c*-SiNW.

(E) High-resolution transmission electron microscope images (TEM) at the interface between the *c*-SiNW wall and ALD-based Al_2O_3. Insets show the fast Fourier transform (FFT) images of *c*-Si and ALD-based Al_2O_3.

doping of *c*-SiNW is not appropriate for high-EQE photodetectors because the *c*-SiNWs are fully depleted with a high doping concentration (>10^{20} cm^{-3}), which causes severe Auger recombination, resulting in degradation of the EQE.[24,25] In other words, most photogenerated carriers in *c*-SiNWs are easily recombined before being collected by the metal electrode. This problem has been successfully addressed by field-induced *p-n* junctions using a conformal ALD-based Al_2O_3 layer on *n*-type *c*-Si.[13–15] The negatively charged ALD-based Al_2O_3 layer has been extensively investigated to replace the conventional thermal doping process. The negatively charged ALD-Al_2O_3 layer pushed electrons back to the *n*-type *c*-Si base and generated a p^+ inversion layer. A schematic of the fabricated *c*-SiNW photodetector based on the field-induced *p-n* junction method is shown in Figure 4A. We designed the same photodiode structure as implemented in our previous work.[13,26] In previous work, a field-induced *p-n* junction was demonstrated as a promising candidate for *c*-Si solar cells with microscale structures. Here, we confirm that the field-induced *p-n* junction is feasible to be applied to *c*-Si photodetectors with nanoscale structures. As discussed in the previous section, a high-quality ALD-Al_2O_3 film was formed on the SiNW surface. We employed MoO_x/Al and LiF/Al electrodes for hole and electron contacts, respectively. Since ALD-Al_2O_3 is a good insulator, the metal electrode cannot make Ohmic contact between the metal and p^+ inversion layer at the surface of *c*-Si if it is directly formed onto ALD-Al_2O_3.[27] We selectively etched the Al_2O_3 layer in the region where metal electrodes were to be formed and deposited molybdenum oxide (MoO_x), which induces a p^+ inversion layer and has high conductivity for holes.[28] LiF is known to lower the contact resistance of *n*-Si/Al, resulting in Ohmic behavior without a doping process.[29]

We measured the current density-voltage (*J-V*) characteristics of the devices with and without ALD-Al_2O_3 under dark and illuminated conditions with a light intensity of 100 mW/cm^2 (Figure S6). The *J-V* curves of the device with ALD-Al_2O_3 clearly exhibited diode characteristics. The diode characteristics could also be observed in devices without ALD-Al_2O_3 owing to the high hole-conductivity and electron-blocking abilities of the MoO_x/Al electrode. However, the photogenerated current of the device without Al_2O_3 (1.81 mA/cm^2) at zero bias is significantly lower than that of the device with Al_2O_3 (8.02 mA/cm^2). This difference explains that most photogenerated carriers are lost due to bulk and front surface recombination because there is no *p-n* junction to separate the photogenerated carriers, which is consistent with our previous photovoltaics work.[13] The measured dark current of the device without Al_2O_3 (3.94×10^{-5} A/cm^2) is also higher than that of the device with Al_2O_3 (1.61×10^{-6} A/cm^2) at zero bias. In other words, ALD-Al_2O_3 induces a *p-n* junction on *c*-SiNWs, which results in efficient carrier separation. The measured dark current is higher than that of commercial devices due to a large contribution of bulk recombination induced by a 375-μm-thick *c*-Si substrate. The *c*-SiNW-based photodetectors were fabricated via conventional thermal doping and field-induced junction methods. Compared to the simulated absorption spectra (Figure 4B), the thermal doping device (Figure 4C) exhibits significantly lower EQEs, regardless of the wire diameter, owing to the severe Auger recombination. In contrast, in the case of the field-induced *p-n* junction device (Figure 4D), the measured EQE exhibits a highly similar trend to the simulated absorption spectra. Furthermore, the EQE peaks of the field-induced *p-n* junction devices are 75.8%, 77.4%, and 77.2%, respectively, owing to the superior capability of the dopant-free *p-n* junction fabricated using

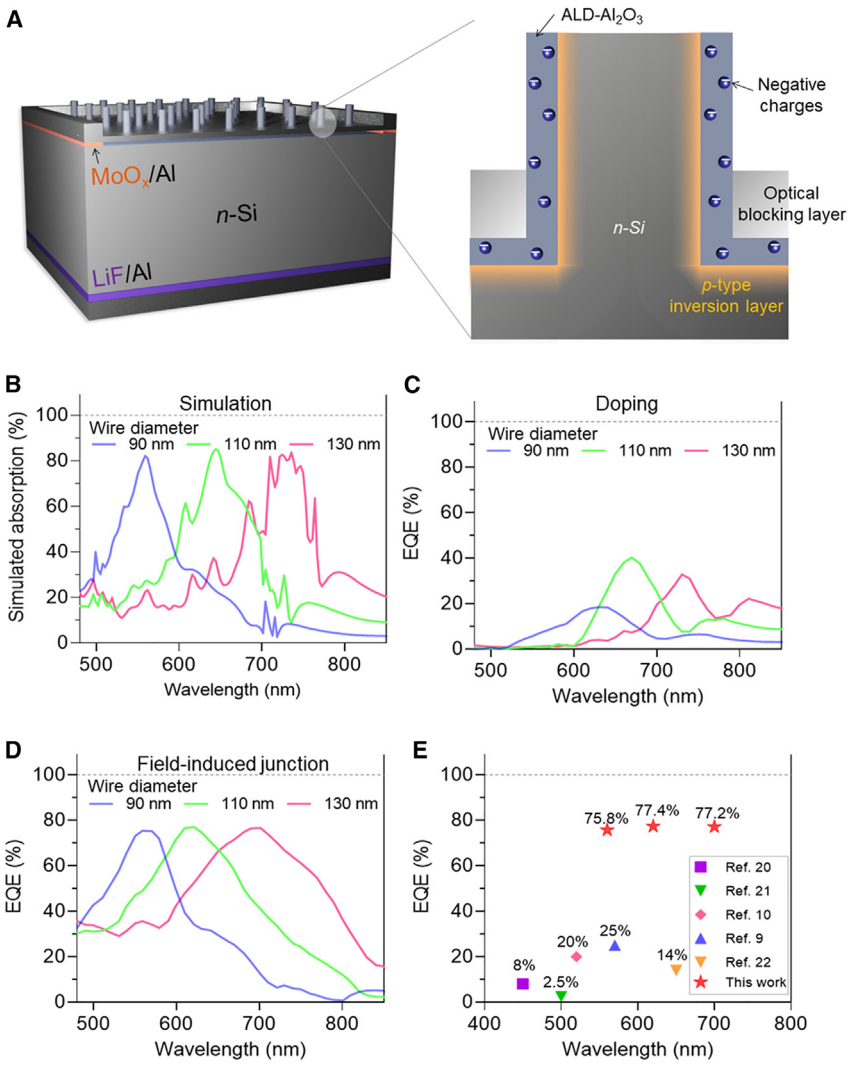

Figure 4. Characterization of *c*-SiNW-based photodetectors with field-induced *p-n* junction and optical blocking layer

(A) Schematic of the structure of the fabricated *c*-SiNW photodetector using ALD-based Al_2O_3.

(B) Simulated absorption spectra of the *c*-SiNW for different diameters.

(C and D) The measured EQE spectra of the *c*-SiNW photodetectors fabricated via (C) thermal doping method and (D) field-induced junction method.

(E) Comparison of the EQE in this study with those of previously reported *c*-SiNW photodetectors.[9,10,21–23]

$ALD\text{-}Al_2O_3$. To the best of our knowledge, this is the highest value among those of previously reported *c*-SiNW-based multispectral photodiodes (Figure 4E; Table S1). Moreover, we compared the measured EQE and simulated absorption before and after applying Al metal as the optical blocking layer, as shown in Figure S7. As demonstrated in the simulation (Figure 2), the selectivity of the photodetector with Al metal is dramatically improved when compared with the EQE spectrum without an optical blocking layer. Therefore, the proposed photodetector with Al metal (optical blocking layer) successfully removed the confounding substrate contribution, as demonstrated by the simulation results.

Furthermore, we fabricated photodetectors for different wire pitches from 500 to 700 nm to further increase the EQE (Figure S8). When the wire pitch was decreased from 700 to 500 nm, only the overall EQE increased; however, the spectrum became broader. This can be explained by the SEM images in Figure S1. The *c*-SiNWs with 500 and 600 nm pitches exhibited a tapered shape compared with those with wider pitches. During DRIE, the wire shape changes extremely sensitively to the gas flow environment. In particular, the etching gas cannot easily penetrate the narrow spacing between *c*-SiNWs.

DISCUSSION

In summary, we developed a wavelength-selective *c*-SiNW photodetector with a maximum EQE of 77.4%. An optical blocking layer and an ALD-based field-induced junction were employed to achieve highly sensitive and wavelength-selective photodetectors. To the best of our knowledge, our photodetectors exhibit the highest EQEs of any of the previously reported *c*-SiNW-based multispectral photodiodes (<30%) at zero bias. We expect that the proposed device architecture can be extended and utilized in numerous nanophotonic research applications. It is expected to be applicable not only to visible wavelength ranges but also to ultraviolet and near-infrared wavelength regions by controlling the wire diameter. Moreover, the fabrication process of the device is compatible with the current complementary metal-oxide-semiconductor fabrication process. In other words, our photodetectors have great potential in various research and industrial fields using optoelectronic platforms such as smartphones, automobiles, drones, and robots.

EXPERIMENTAL PROCEDURES

Resource availability

Lead contact

Further information and requests for resources should be directed to and will be fulfilled by the lead contact, Prof. Kwanyong Seo (kseo@unist.ac.kr).

Materials availability

This study did not generate new materials.

Data and code availability

The raw data are available from the lead contact (kseo@unist.ac.kr) upon reasonable request.

FDTD simulation

The FDTD simulations were performed using the Lumerical FDTD software package. *c*-SiNW arrays were developed using a 3D rectangular simulation

region with periodic boundary conditions along the x and y axes. To construct a square lattice of the *c*-SiNW array, a single *c*-SiNW was located at the center (top view) of the square simulation region. The bottom *c*-Si substrate was placed beneath the *c*-SiNW, and infinite boundary conditions, rendered as PML, were applied along the z axis. The lattice of the array was adjusted according to the x and y span. The Palik material data provided by Lumerical were used to model the material as Si. Simulations were performed in the wavelength range of 450–900 nm using a plane-wave light source. The wire absorption was obtained using an advanced power absorption monitor in FDTD. The bottom *c*-Si substrate absorption was calculated using a 2D *z*-normal monitor at the interface between *c*-SiNW array and substrate.

Fabrication of *c*-SiNW array

c-SiNW array on an *n*-type Czochralski (CZ) Si(100) wafer (resistivity: 1−3 Ω cm) was successively cleaned with acetone and isopropyl alcohol (IPA). Two different e-beam resists (495 PMMA A2 and 950 PMMA A2, MicroChem) were used for the e-beam lithography process. On the cleaned substrate, 495 PMMA A2 was coated first at the speed of 4,000 rpm for 60 s and then annealed the substrate at 180°C for 10 min. Upon cooling for 10 min at room temperature, 950 PMMA A2 was coated under the same spin-coating and annealing conditions. E-beam lithography (nB3, NanoBeam) was conducted at a dose of 11.7 C/m^2 with a beam current of 0.7 nA to produce disk array patterns. Typically, each array comprises an area of 100 × 100 μm. The patterns for the photodetector devices had an area of 200 × 200 μm. The diameter of the disks ranged from 150 to 180 nm in steps of 20 nm. The exposed e-beam resist was developed in a 1:3 MIBK:IPA solution for 90 s and then rinsed in IPA for 30 s. An etching mask of 50-nm-thick Al was deposited using a thermal evaporator, and the lift-off process was performed using an acetone solution for 6 h. The vertical *c*-SiNW arrays were fabricated in the DRIE with a source power of 1,200 W, a stage power of 12 W, and a chamber pressure of 7.5 mTorr at 20°C. We used 55 sccm SF_6 and 130 sccm C_4F_8 gas. Following etching, the deposited Al metal mask was removed using a mixture of sulfuric acid and hydrogen peroxide (H_2SO_4:H_2O_2 = 3:1). The diameter of the fabricated *c*-SiNW arrays was reduced by dry oxidation and wet etching processes. We ramped the furnace temperature up to 1,100°C while 125 sccm N_2 gas flowed continuously. Once the temperature reached 1,100°C, only 500 sccm O_2 gas flowed for 60 min at the same temperature. Subsequent buffered oxide etchant (BOE; HF:NH_4F = 7:1) treatment removed the oxide layer approximately 30 nm in size uniformly. The final target diameters ranged from 90 to 130 nm in steps of 20 nm.

Fabrication of *c*-SiNW photodetector with optical blocking layer

We deposited 10 nm Al_2O_3 onto the SiNW arrays using ALD (Lucida D200, NCD), followed by annealing under 500 sccm Ar at 500°C for 30 min. Subsequently, 10 nm Al_2O_3 was grown at 200°C using 86 cycles of trimethylaluminum (TMA) and deionized (DI) water pulses. The ALD cycle contained the following processing sequence: 0.2 s TMA pulse, 15 s N_2 purge, 0.2 s DI water pulse, and 15 s N_2 purge. During the Al_2O_3 deposition, the N_2 gas flow rate was maintained at 50 sccm. Al (50 nm) was deposited via thermal evaporation. A DPR-i1549 PR was spin coated onto the *c*-SiNW array at 2,000 rpm for 30 s. The sample was baked at 105°C for 4 min, and the PR thickness was 3.6 μm as confirmed by SEM measurements. Oxygen plasma etching (V15-G, Plasma Finish) was conducted at a plasma power of 500 W and a 60 mL/min O_2 flow rate for 400 s at a base pressure of 50 Pa. Subsequently, the Al films on the flat top and sidewalls were selectively etched using AZ 300 MIF (developer). Finally, an oxygen plasma etching treatment was conducted to remove the remaining PR. Patterns for the metal electrode were lithographically defined on the front of the samples using DPR-i1549 PR. To fabricate the electrodes, the substrates were dipped in BOE solution, and 10/200 nm MoO_x/Al films were thermally evaporated on their front surfaces. Similar to the previous instance, lift off was performed by immersion in acetone solution to remove the undesired metal. Finally, 1/200 nm LiF/Al electrodes were deposited on the rear of the substrates.

Characterization of photodetector

The EQE spectra of the fabricated photodetectors were measured using IQE-200B (Newport). The beam size was 1 × 1 mm. The area of the fabricated photodetector was 200 × 200 μm, which is one-quarter of the beam size. Calibration was performed using an NREL-calibrated solar cell (PV Measurements) with an Al mask (aperture size: 200 × 200 μm). Moreover, we rechecked the fabricated *c*-Si solar cells. The active areas of the fabricated solar cells were 200 × 200 μm and 1 × 1 cm. The active areas were defined using Al metal electrodes. We compared the EQE spectra of the fabricated solar cells with different active areas.

SUPPLEMENTAL INFORMATION

Supplemental information can be found online at https://doi.org/10.1016/j.device.2023.100018.

ACKNOWLEDGMENTS

This work was supported by National Research Foundation of Korea (NRF) grants funded by the Korean Government (MSIP) (NRF-2019R1A2C20806602, NRF-2019M1A2A2065614, NRF-2022R1C1C2004320, NRF-2021R1F1A1064243, and NRF- 2022R1C1C1010025). This work was supported by the 2023 research fund (1.230040.01) of the Ulsan National Institute of Science and Technology (UNIST). This research used high-performance computing resources of the UNIST Supercomputing Center.

AUTHOR CONTRIBUTIONS

D.C. and J.L. contributed equally to this work. K.S. and D.C. conceived the idea of the field-induced junction. K.S. and M.W. conceived the idea of a metal blocking layer. D.C., M.W., and K.S. designed the experiments. D.C. and J.L. performed device fabrication and characterization. D.C. performed FDTD simulations. K.S., H.-D.U., and M.W. performed the FDTD simulation analysis. Y.-K.K. performed the TEM measurements and analyses. D.C. and K.S. wrote the paper, and all other authors commented on the manuscript.

DECLARATION OF INTERESTS

The authors declare no competing interests.

Received: April 4, 2023
Revised: June 9, 2023
Accepted: July 7, 2023
Published: August 1, 2023

REFERENCES

1. Park, H., Park, H., Chung, H.Y., O, T.M., and Waner, M. (2015). Vertically stacked photodetector devices containing silicon nanowires with engineered absorption spectra. ACS Photonics *42*, 544–551. https://doi.org/10.1021/ph500463r.
2. Tian, B., Zheng, X., Kempa, T.J., Fang, Y., Yu, N., Yu, G., Huang, J., and Lieber, C.M. (2007). Coaxial silicon nanowires as solar cells and nanoelectronic power sources. Nature *449*, 885–889. https://doi.org/10.1038/nature06181.
3. Oener, S.Z., Cavalli, A., Sun, H., Haverkort, J.E.M., Bakkers, E.P.A.M., and Garnett, E.C. (2018). Charge carrier-selective contacts for nanowire solar cells. Nat. Commun. *9*, 3248. https://doi.org/10.1038/s41467-018-05453-5.
4. Garnett, E., and Yang, P. (2010). Light trapping in silicon nanowire solar cells. Nano Lett. *10*, 1082–1087. https://doi.org/10.1021/nl100161z.
5. Kelzenberg, M.D., Turner-Evans, D.B., Kayes, B.M., Filler, M.A., Putnam, M.C., Lewis, N.S., and Atwater, H.A. (2008). Photovoltaic measurements in single-nanowire silicon solar cells. Nano Lett. *8*, 710–714. https://doi.org/10.1021/nl072622p.
6. Um, H.-D., Choi, D., Choi, A., Seo, J.H., and Seo, K. (2017). Embedded Metal Electrode for Organic–Inorganic Hybrid Nanowire Solar Cells. ACS Nano *11*, 6218–6224. https://doi.org/10.1021/acsnano.7b02322.
7. Cadusch, J.J., Meng, J., Craig, B., and Crozier, K.B. (2019). Silicon microspectrometer chip based on nanostructured fishnet photodetectors with

tailored responsivities and machine learning. Optica *6*, 1171–1177. https://doi.org/10.1364/optica.6.001171.

8. Seo, K., Wober, M., Steinvurzel, P., Schonbrun, E., Dan, Y., Ellenbogen, T., and Crozier, K.B. (2011). Multicolored vertical silicon nanowires. Nano Lett. *11*, 1851–1856. https://doi.org/10.1021/nl200201b.
9. Um, H.D., Solanki, A., Jayaraman, A., Gordon, R.G., and Habbal, F. (2019). Electrostatically Doped Silicon Nanowire Arrays for Multispectral Photodetectors. ACS Nano *13*, 11717–11725. https://doi.org/10.1021/acsnano.9b05659.
10. Meng, J., Cadusch, J.J., and Crozier, K.B. (2020). Detector-only spectrometer based on structurally colored silicon nanowires and a reconstruction algorithm. Nano Lett. *20*, 320–328. https://doi.org/10.1021/acs.nanolett.9b03862.
11. Liu, X., Coxon, P.R., Peters, M., Hoex, B., Cole, J.M., and Fray, D.J. (2014). Black silicon: Fabrication methods, properties and solar energy applications. Energy Environ. Sci. *7*, 3223–3263. https://doi.org/10.1039/C4EE01152J.
12. Allen, F.I. (2021). A review of defect engineering, ion implantation, and nanofabrication using the helium ion microscope. Beilstein J. Nanotechnol. *12*, 633–664. https://doi.org/10.3762/bjnano.12.52.
13. Choi, D., and Seo, K. (2021). Field-Induced Radial Junction for Dopant-Free Crystalline Silicon Microwire Solar Cells with an Efficiency of Over 20. Adv. Energy Mater. *11*, 2003707. https://doi.org/10.1002/aenm.202003707.
14. Juntunen, M.A., Heinonen, J., Vähänissi, V., Repo, P., Valluru, D., and Savin, H. (2016). Near-unity quantum efficiency of broadband black silicon photodiodes with an induced junction. Nat. Photonics *10*, 777–781. https://doi.org/10.1038/nphoton.2016.226.
15. Garin, M., Heinonen, J., Werner, L., Pasanen, T.P., Vähänissi, V., Haarahiltunen, A., Juntunen, M.A., and Savin, H. (2020). Black-Silicon Ultraviolet Photodiodes Achieve External Quantum Efficiency above 130. Phys. Rev. Lett. *125*, 117702. https://doi.org/10.1103/PhysRevLett.125.117702.
16. Khaidarov, E., Eschimese, D., Lai, K.H., Huang, A., Fu, Y.H., Lin, Q., Paniagua-Dominguez, R., and Kuznetsov, A.I. (2022). Large-scale vivid metasurface color printing using advanced 12-in. immersion photolithography. Sci. Rep. *12*, 14044. https://doi.org/10.1038/s41598-022-18259-9.
17. Henyey, F.S. (1982). Distinction between a perfect conductor and a superconductor. Phys. Rev. Lett. *49*, 416. https://doi.org/10.1103/PhysRevLett.49.416.
18. Lindell, I.V., and Sihvola, A.H. (2005). Perfect electromagnetic conductor. J. Electromagn. Waves Appl. *19*, 861–869. https://doi.org/10.1163/156939305775468741.
19. Loo, Y.L., Willett, R.L., Baldwin, K.W., and Rogers, J.A. (2002). Interfacial chemistries for nanoscale transfer printing. J. Am. Chem. Soc. *124*, 7654–7655. https://doi.org/10.1021/ja026355v.
20. Afanas'ev, V.V., Stesmans, A., Mrstik, B.J., and Zhao, C. (2002). Impact of annealing-induced compaction on electronic properties of atomic-layer-deposited Al2O3. Appl. Phys. Lett. *81*, 1678–1680. https://doi.org/10.1063/1.1501163.
21. Park, H., Dan, Y., Seo, K., Yu, Y.J., Duane, P.K., Wober, M., and Crozier, K.B. (2014). Filter-free image sensor pixels comprising silicon nanowires with selective color absorption. Nano Lett. *14*, 1804–1809. https://doi.org/10.1021/nl404379w.
22. Park, H., and Crozier, K.B. (2015). Elliptical silicon nanowire photodetectors for polarization-resolved imaging. Opt Express *23*, 7209–7216. https://opg.optica.org/abstract.cfm?URI=oe-23-6-7209.
23. Li, S.Q., Solanki, A., Frigerio, J., Chrastina, D., Isella, G., Zheng, C., Ahnood, A., Ganesan, K., and Crozier, K.B. (2019). Vertical Ge-Si Nanowires with Suspended Graphene Top Contacts as Dynamically Tunable Multispectral Photodetectors. ACS Photonics *6*, 735–742. https://doi.org/10.1021/acsphotonics.8b01646.
24. Richter, A., Glunz, S.W., Werner, F., Schmidt, J., and Cuevas, A. (2012). Improved quantitative description of Auger recombination in crystalline silicon. Phys. Rev. B *86*, 165202. https://doi.org/10.1103/PhysRevB.86.165202.
25. Cuevas, A., Basore, P.A., Giroult-Matlakowski, G., and Dubois, C. (1996). Surface recombination velocity of highly doped n-type silicon. J. Appl. Phys. *80*, 3370–3375. https://doi.org/10.1063/1.363250.
26. Choi, D., Yoon, H., Kim, K.H., Um, H.D., and Seo, K. (2019). ITO-free carrier-selective contact for crystalline silicon solar cells. J. Mater. Chem. A Mater. *7*, 2192–2199. https://doi.org/10.1039/C8TA11220G.
27. Filatova, E.O., and Konashuk, A.S. (2015). Interpretation of the Changing the Band Gap of Al_2O_3 Depending on Its Crystalline Form: Connection with Different Local Symmetries. J. Phys. Chem. C *119*, 20755–20761. https://doi.org/10.1021/acs.jpcc.5b06843.
28. Battaglia, C., Yin, X., Zheng, M., Sharp, I.D., Chen, T., McDonnell, S., Azcatl, A., Carraro, C., Ma, B., Maboudian, R., et al. (2014). Hole Selective MoO_x Contact for Silicon Solar Cells. Nano Lett. *14*, 967–971. https://doi.org/10.1021/nl404389u.
29. Bullock, J., Zheng, P., Jeangros, Q., Tosun, M., Hettick, M., Sutter-Fella, C.M., Wan, Y., Allen, T., Yan, D., Macdonald, D., et al. (2016). Lithium Fluoride Based Electron Contacts for High Efficiency n-Type Crystalline Silicon Solar Cells. Adv. Energy Mater. *6*, 1600241. https://doi.org/10.1002/aenm.201600241.